Modeling tsunami and seismic waveforms from regional earthquakes to inform system design and data integration for the Tamtam SMART subsea cable

Kwok Fai Cheung[1], Yoshiki Yamazaki[1], Thorne Lay[2], Matthew J. Fouch[3], John Jr. Niroa[4], and Bruce M. Howe[1]

[1]Department of Ocean and Resources Engineering, University of Hawaii at Manoa, Honolulu, Hawaii, 96822, USA
[2]Department of Earth and Planetary Sciences, University of California Santa Cruz, Santa Cruz, California, 95064, USA
[3]Subsea Data Systems, Washington DC, USA
[4]Vanuatu Meteorology and Geo-hazards Department, Port Vila, Vanuatu

Correspondence to: Kwok Fai Cheung (cheung@hawaii.edu)

Abstract. Science Monitoring And Reliable Telecommunications (SMART) subsea cables utilize sensors integrated within repeaters to record temperature, acceleration, and pressure on the seafloor. The planned Tamtam SMART cable will connect Vanuatu and New Caledonia across a major subduction zone. Modeling recent *Mw* 7.7 to 8.0 earthquakes and maximum considered *Mw* 8.33 to 8.8 scenarios provides a range of seismic waveforms with realistic relative timing and long-period ground displacements at the sensor locations as well as coseismic seafloor uplift and subsidence at the sources used for tsunami excitation. A nonhydrostatic model describes tsunami generation, propagation, and scattering in the southwest Pacific. Spectral analysis of the computed tsunami waves shows multi-scale oscillations along the Vanuatu trench with periods from a few minutes to over an hour. The cable sensor locations are outside energetic antinodes of oscillation modes and the modeled tsunami amplitude is representative of the seismic source with minor interference from land masses. The suite of synthetic seismic and tsunami waveforms informs implementation of the sensor system for regional hazard monitoring. The Tamtam SMART cable, deployed in a very active tectonic environment with limited on-land instrumentation, will augment rapid earthquake and tsunami warning as well as source quantification.

1. Introduction

The last decade has seen increased interest in leveraging subsea telecommunication cables as a cost-effective means to monitor vast expanses of the ocean. There are currently 1.5 million kilometers of subsea cables in operation around the world. When existing cables are replaced or

32 new routes are planned, sensors can be installed at repeaters or in separate modules to provide

33 dense measurements of temperature, acceleration, and pressure for oceanographic and climate

34 research at a modest incremental cost (Howe et al., 2019). The resulting Science Monitoring And

35 Reliable Telecommunications (SMART) subsea cables can also provide real-time data for

36 earthquake and tsunami early warning, and that has provided motivation for a number of on-going

37 projects, such as the InSEA wet demonstration project off Sicily, Italy; and the Atlantic CAM ring

38 system connecting Lisbon, Azores, and Madeira in Portugal (Howe et al., 2022).

39 Planning for the Tamtam SMART subsea cable between Vanuatu and New Caledonia in the

40 Southwest Pacific is currently underway. The system will stretch across the Vanuatu subduction

41 zone, which is very active and geologically young with frequent tsunamigenic earthquakes (Roger

42 and Pelletier, 2024). The planned cable route extends from Port Vila, the capital of Vanuatu on

43 Efate Island, along the archipelago to the south before crossing the trench to reach an existing

44 landing station on Lifou Island with connectivity to the rest of New Caledonia (Fig. 1). There are

45 four sensor modules 50~90 km apart along the 450 km cable. Three sensor modules are planned

46 for the upper margin slope along the shelf edge and one at the trench to provide real-time

47 earthquake and tsunami monitoring capability near populated areas. This project is situated in a

48 region with existing seismic and sea level networks that can provide information for examination

49 of data quality and interoperability. As shown in Fig. 1a, the New Zealand DART (Detection and

50 Reporting of Tsunami) network has some coverage of tsunami waves in the Southwest Pacific

51 with stations to the west and south of the Vanuatu islands (Fry et al., 2020). Global seismic network

52 stations are rather sparsely distributed in the Southwest Pacific but are supplemented by more than

53 50 stations of the Oceania Regional Seismic Network (ORSNET) operated by South Pacific

54 countries (UNESCO-IOC, 2025).

55 Tsunamis in the region have been generated predominantly by earthquakes with volcanic and

56 non-seismic sources representing less than 5% of documented events (Roger and Pelletier, 2024).

57 Fig. 1b shows the locations of selected tsunamigenic earthquakes with regional implications. The

58 northern Vanuatu subduction zone has produced several large earthquakes in the past century. One

59 of the largest is the 6 February 2013 Mw 8.0 Santa Cruz Islands thrust faulting with shallow

60 eastward dip that generated a destructive tsunami impacting local communities (e.g., Lay et al.,

61 2013; Cleveland et al., 2014). Across the d'Entrecasteaux Ridge, the southern Vanuatu subduction

62 zone is known for strong and long-duration aftershock sequences (Ye et al., 2021), accompanying

63 major plate boundary and outer rise earthquakes (Roger et al., 2021). The largest, 1875 thrust-

64 faulting earthquake with estimated *Mw* 8.1-8.2 produced sediment deposits reaching 10 m

65 elevation on the northeastern coast of Lifou Island, New Caledonia (Paris et al., 2023), while an

66 *Mw* 7.7 normal faulting event in May 1995 along the Loyalty ridge generated a tsunami with 8 m

67 runup on Aneityum Island, Vanuatu (Roger and Pelletier, 2024).

68
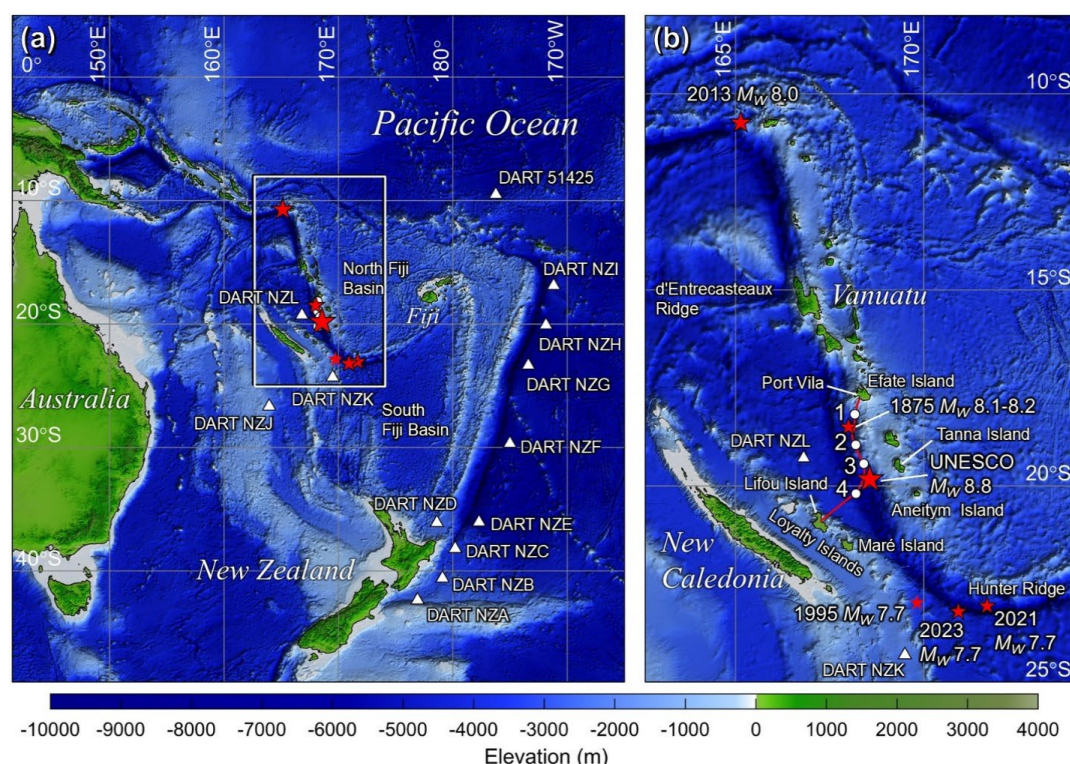
Figure 1. Location map and two levels of nested computational grids. (a) Level-1 Southwest
Pacific. White rectangle indicates the level-2 grid coverage. (b) Level-2 Vanuatu subduction zone.
The magenta line and white circles denote planned SMART cable and sensor locations. White
triangles denote DART locations. Smaller red stars indicate epicenters of large historical and
recent tsunamigenic earthquakes and the large red star indicates the maximum earthquake in the
Southern Vanuatu Subduction Zone from UNESCO-IOC (2025).

75   The southernmost Vanuatu Trench curves eastward along the Hunter Ridge. The two largest

76 *Mw* 7.7 earthquakes in the past quarter-century occurred on opposing sides of the Southern

77 Vanuatu Trench in 2021 and 2023. The resulting tsunamis of similar wave amplitude have distinct

78 near-field patterns associated with the source location in relation to nearby seamounts and islands,

79 but similar far-field patterns due to standing waves amongst the many seamounts and islands in

80   the southwest Pacific (Robert et al., 2025). This event pair within 2 years is analogous to the 2013

81   Santa Cruz megathrust *Mw* 8.0 and 2015 normal faulting *Mw* 7.0 earthquakes on opposing sides of

82   the trench in the northern Vanuatu subduction zone (Heidarzadeh et al., 2016). These recent

83   earthquakes at the northern and southern termini of the subduction zone produced moderate

84   tsunamis affecting Vanuatu and New Caledonia. Larger historical earthquakes between the two

85   island chains, such as the 1875 *Mw* 8.1-8.2 and the 1995 *Mw* 7.7, indicate greater tsunami risk to

86   population centers. Port Vila was extensively damaged by ground shaking from a nearby 54 km

87   deep *Mw* 7.3 intraslab event in December 2024, accompanied by a minor tsunami of 0.25 m

88   amplitude.

89   Governments, scientists, and stakeholders are motivated to understand earthquake and tsunami

90   hazards to support comprehensive risk management strategies among nations in the Southwest

91   Pacific. UNESCO-IOC (2025) proposed maximum earthquake scenarios inferred probabilistically

92   from the estimated degree of segmentation, width of strain accumulation zones, fault locking

93   relative to plate convergence, and material properties of rocks along the Vanuatu subduction zone.

94   Comparable maximum earthquake estimates were made for the northern, central, southern, and

95   Matthew-Hunter Islands regions along the arc. Full rupture of the southern 500-km long segment,

96   where the proposed Tamtam SMART cable is located, can produce up to *Mw* 8.8 involving five

97   *Mw* 8.33 subevents. These scenarios along with the well-resolved 2013 *Mw* 8.0 Santa Cruz Islands

98   earthquake to the north and the 2021 and 2023 *Mw* 7.7 earthquakes southeast of the Loyalty Islands

99   provide a range of large events in the region that the proposed SMART subsea cables might record

100   signals for (Fig. 1b). Modeling the corresponding earthquake and tsunami signals can inform

101   system and sensor design, aid data integration into regional networks, and identify implications

102   for emergency management in the cable system planning stage.

2. Tsunami and seismic wave modeling

104   Finite fault-slip models have been an effective tool to describe earthquake rupture and seafloor

105   deformation time histories for non-hydrostatic modeling of tsunami generation (Yamazaki et al.,

106   2023). The methodology has evolved over the last half-century from simple point source models

107   in homogenous, elastic half-space to space-time distributions of slip over a finite-fault surface or

108   network of surfaces, constrained by combinations of seismic, geodetic, and tsunami observations.

109 Such models are now routinely obtained for large earthquakes, and can be used in quantitative

110 forward modeling of long-period ground motions at any location of interest.

2.1 Rupture models

112   Finite fault-slip models describe rupture kinematics through grids of subfaults, each of which

113 has uniform slip and a parameterized source time function. The collective motion accounts for the

114 spatial-temporal seismic moment and energy release during the rupture. In our present formulation,

115 the seafloor vertical displacement is computed from the half-space solution of Okada (1985) and

116 adjusted for horizontal translation of the local slope according to Tanioka and Satake (1996). Fig.

117 2 shows the finite fault-slip models and co-seismic vertical seafloor displacement for the 2013 M_W

118 8.0 Santa Cruz Islands earthquake (Lay et al., 2013), the 2021 and 2023 M_W 7.7 earthquakes

119 southeast of the Loyalty Islands (Robert et al., 2025), and the M_W 8.8 maximum considered

120 earthquake scenario for the southern Vanuatu subduction zone (UNESCO-IOC, 2025). The three

121 historical events have finer subfaults that provide fairly detailed slip distributions and time

122 histories inferred from global seismic and regional tsunami wave recordings, valid for seismic

123 periods longer than ~5-10 s. The maximum earthquake scenario has larger subfaults with

124 prescribed uniform slip and rise time, and is only valid for seismic periods longer than ~15 s.

125   The 2013 M_W 8.0 Santa Cruz Islands earthquake has shallow eastward dip in two large slip

126 patches and a southeastward rupture expansion at ~1.5 km/s. The megathrust rupture has up to

127 12.7 m slip producing 3.3 m near-trench uplift and minor arc subsidence (Lay et al., 2013). The

128 2021 M_W 7.7 thrust-faulting earthquake occurred at the plate boundary interface near the southern

129 hook of the Vanuatu subduction zone. The peak slip reaches 7.5 m over a 55 s rupture time and

130 produces 1.3 m uplift and minor subsidence on the lower and upper margin slope (Robert et al.,

131 2025). The nearby 2023 M_W 7.7 earthquake with a similar east-west extent involved a normal fault

132 in the outer rise. The peak slip reaches 5.2 m over a 45 s rupture time with relatively small uplift

133 but large subsidence of 2.4 m near the trench (Robert et al., 2025). The finite fault models for the

134 three historical events, which have been determined from joint seismic and tsunami modeling, are

135 implemented to provide time histories of seafloor deformation for tsunami excitation directly.

136 Short-period features of the sources and details of the propagation structures are not known, so we

137 restrict our seismic modeling near the Tamtam sites to ground displacements with long-periods

138 consistent with simplified, point-source model representations in a one-dimensional velocity

139 structure.
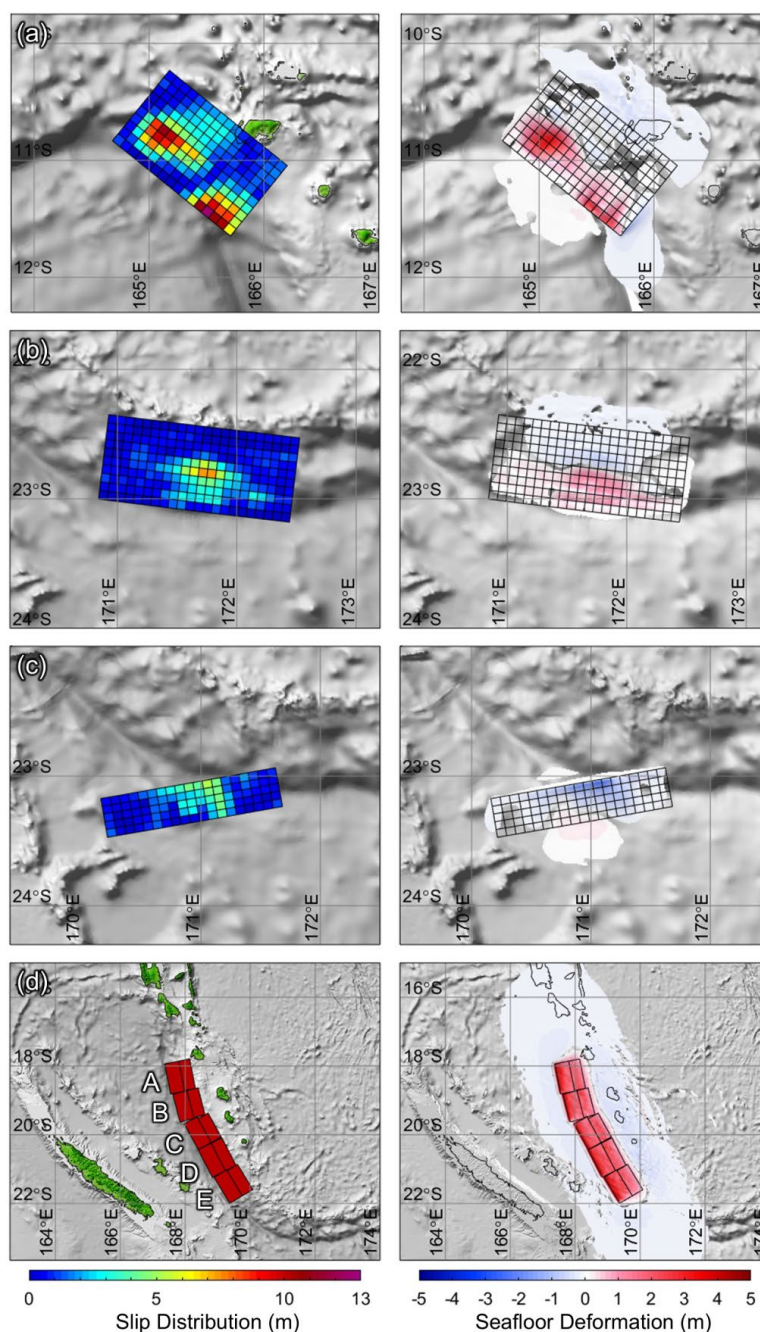
Figure 2. Slip distribution and seafloor deformation. (a) The 2013 Mw 8.0 Santa Cruz Islands earthquake. (b) The 2021 Mw 7.7 earthquake southeast of the Loyalty Islands. (c) The 2023 Mw 7.7 earthquake southeast of the Loyalty Islands. (d) UNESCO Mw 8.33 A, B, C, D, and E sub-events which combine to give the Mw 8.8 earthquake scenario.

145   The rupture of the maximum considered earthquake scenario extends 500 km along the
146   southern Vanuatu subduction zone and 100 km downdip from the trench (UNESCO-IOC, 2025).
147   The M_W 8.8 earthquake scenario corresponds to the 90th percentile in the posterior maximum
148   moment distribution of the probabilistic tsunami hazard assessment compiled by Davis and Griffin
149   (2018). The model has uniform slip of 10 m and a rigidity of 40 GPa. The slip is within the range
150   of the three recent major events from 5.2 to 12.7 m, but is implemented over a much larger area
151   for the maximum scenario. The uplift varies gradually from 1.1 m at the shelf edge to 4.6 m near
152   the trench and the subsidence is relatively small due to the uniform slip across the full segment.
153   The five M_W 8.33 subevents on 100 km wide and 100 km long ruptures can be considered
154   separately as local failures along the segment to augment the parameter space. Each subevent is
155   comparable to the largest observed, 1875 M_W 8.1-8.2 earthquake in the region (Ioualalen et al.,
156   2017). For modeling of tsunami excitation, the rupture is assumed to start simultaneously across
157   the entire fault and the dislocation follows a linear ramp function over a 30 sec rise time to reach
158   the specified total slip. There is no known constraint on rupture heterogeneity or directivity.
159   Simultaneous rupture of the five subevents is computed for the M_W 8.8 earthquake scenario to
160   direct tsunami waves normal to the arc and to provide a conservative estimate of the resulting
161   impact to local communities on either side.

162   **2.2 Tsunami modeling**

163   The tsunami code NEOWAVE augments the commonly used nonlinear shallow-water
164   equations with depth-averaged vertical velocity and non-hydrostatic pressure (Yamazaki et al.,
165   2009, 2011). The resulting quasi three-dimensional flow can describe tsunami generation from
166   time-dependent seafloor deformation, frequency dispersion during trans-oceanic propagation, and
167   wavenumber-dependent shoaling on seafloor slopes. The vertical inertia in the nonhydrostatic
168   formulation facilitates accurate description of sea-surface oscillation at tsunami sources as well as
169   runup and drawdown on steep topography (Bai et al., 2023). A shock-capturing scheme
170   approximates breaking waves as bores or hydraulic jumps to ensure conservation of mass and
171   momentum while enabling energy dissipation without predefined empirical mechanisms. These
172   model capabilities have been benchmarked against mathematical and numerical models as well as
173   laboratory and field measurements (Yamazaki et al., 2023).

174   The modeling involves two levels of two-way nested computational grids telescoping from the
175   Southwest Pacific to the tsunami source region along the Vanuatu subduction zone. The digital

176   elevation model is derived from GEBCO14 at 30 arcsec (~0.9 km). The level-1 grid covers the

177   Southwest Pacific to capture large-scale standing waves generated by reflection from land masses

178   as well as trapping along island chains (Fig. 1a). The 2-arcmin (~3.7 km) resolution leads to

179   optimal model dispersion for transoceanic tsunami propagation (Li and Cheung, 2019). As shown

180   in Fig. 1b, the level-2 grid extends along the Vanuatu subduction zone and resolves the margin

181   and tsunami sources at 30 arcsec (~0.9 km). The co-seismic seafloor vertical displacement defines

182   the tsunami excitation and updates the digital elevation model. Inundation is not modeled at this

183   resolution and the subgrid roughness of the seafloor is described by a Manning's number of 0.025.

184   The local mean-sea level is the datum of the digital elevation model as well as the sea surface

185   elevation.

2.3 Seismic wave modeling

187   Dynamic ground motions are computed at a target location (18.782°S, 168.2°E), which is

188   planned for sensor 2 on the Tamtam SMART cable (Fig. 1b). The predicted ground motions vary

189   slowly in space and thus remain very similar at the four sensor locations. The purpose here is to

190   inform sensor design and data integration by estimating approximate timing, duration, and levels

191   of long period ground displacement produced near the site for large recent plate boundary and

192   plausible maximum regional ruptures along the Vanuatu subduction zone. The precise details of

193   the historical, finite-fault ruptures are not important here and are unknown for maximum rupture

194   scenarios. Numerical modeling is thus simplified to computation of equivalent point-source

195   representations of the three large recent events and the subevents of the maximum rupture scenario

196   along with their composite.

197   Synthetic seismograms are computed using a standard one-dimensional Earth Model, which is

198   an anisotropic version of the Preliminary Reference Earth Model (PREM; Dziewonski and

199   Anderson, 1981). The ground displacements up to 2 s period are computed using the SYNGINE

200   (synthetic engine) seismic wave simulator (https://ds.iris.edu/ds/products/ondemandsynthetics/),

201   for point-source moment tensor representations of the earthquake models. While short-period

202   seismic waves and associated ground velocities and accelerations will be affected by the actual

203   three-dimensional structure along the paths from sources to the observing location, the details are

204   not known for this particular assessment of the ground shaking levels. Our focus is on the relative

205   timing, duration, and amplitude of long period ground displacements produced by each source near

206   the Tamtam site.

3. Model results

The modeling work provides tsunami and seismic waves generated by the three recent major earthquakes and the UNESCO maximum scenario including its five subevents along the Vanuatu subduction zone. The tsunami modeling covers an elapsed time of 10 hours to capture shelf oscillations along the archipelago as well as standing waves within the north and south Fiji Basins. The results include regional tsunami amplitude maps, energetic oscillation modes along the margin, and synthetic tsunami and seismic waveforms at the representative, sensor 2 location of the planned SMART subsea cable.

3.1 Recent major events

The 2013 *Mw* 8.0 Santa Cruz Islands earthquake and the 2021 and 2023 *Mw* 7.7 earthquakes southeast of the Loyalty Islands are representative of major events from the northern and southern termini of the Vanuatu subduction zone. Fig. 3 shows regional distributions of the maximum sea surface excursion, which includes crest and trough amplitude to better represent the energy pattern, especially for the 2023 normal-fault event (Robert et al., 2025). The two near-trench uplift patches from the 2013 thrust faulting provide the primary source of the tsunami with minor contributions from subsidence on the upper margin slope (Fig. 2a). Constructive interference of the radiated waves from the two uplift patches defines the main lobes in the northeast and southwest directions away from Vanuatu (Fig. 3a). Refraction of the radiated waves over the margin slope and outer rise produces notable side lobs to the east and south toward the Santa Cruz Islands and the main island of New Caledonia, respectively. The SMART cable site located southeast of the source on the margin slope experience only minor wave action albeit with amplification over adjacent insular shelves along the Vanuatu Islands.

The 2021 and 2023 *Mw* 7.7 earthquakes on opposing sides of the southern Vanuatu Trench have similar east-west rupture extents, but produce tsunamis with a leading crest and a leading trough associated with the thrust and normal faulting mechanisms, respectively (Robert et al., 2025). The distinct northern energy lobes result from the source location relative to seamounts and islands immediately north along the Hunter Ridge. In comparison, the southern lobes are normal to the strike of the respective earthquakes due to lack of major bathymetric features south of the source. The 2023 earthquake has narrower seafloor deformation beneath deeper water resulting in shorter period tsunami waves that are focused more effectively along seamounts and island chains to produce a more elaborate wave pattern. Both tsunamis generated by earthquakes in the southern

238   arc of the subduction zone direct the primary energy to the north and south with minimal threat to

239   the main island of New Caledonia. Refraction of the radiated waves over the margin slope

240   generates side lobes toward the Vanuatu Islands with moderate wave action associated with shelf

241   oscillations for both events.
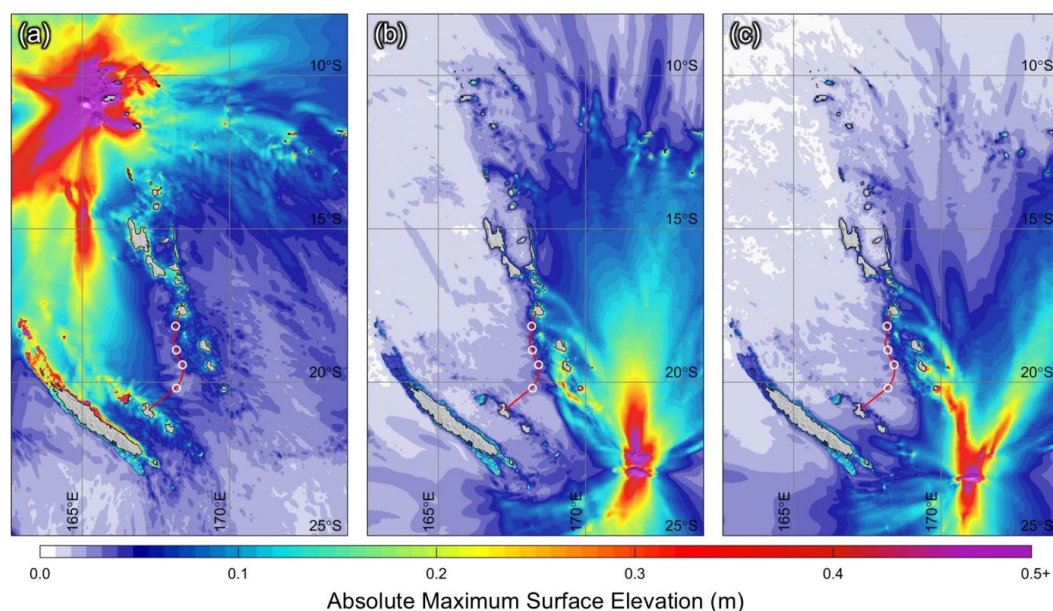
242
243   **Figure 3.** Computed absolute maximum surface elevation of tsunamis generated by recent major
244   earthquakes. (a) The 2013 M_W 8.0 Santa Cruz Islands earthquake. (b) The 2021 M_W 7.7 Southeast
245   of Loyalty Islands earthquake. (c) The 2023 M_W 7.7 Southeast of Loyalty Islands earthquake. Red
246   line and circles denote planned SMART cable and sensor locations.

247   The four planned sensor modules are located off the insular shelves (Fig. 1b) and outside zones

248   of tsunami amplification for all three recent events (Fig. 3). The computed sea-surface elevations

249   at the sensors are an order of magnitude smaller compared to the adjacent shallow shelves. The

250   bathymetry-driven oscillation is illustrated by spectral analysis of the computed 2013 tsunami that

251   converts the surface elevation time history to amplitude as a function of period (Munger and

252   Cheung, 2008). Fig. 4 shows selected oscillation modes with well-defined nodal lines, where the

253   amplitude is zero and the phase varies by 180º across indicative of resonance. The 7 to 40-min

254   modes indicate distinct standing edge waves along the New Caledonia ridge, the Loyalty Island

255   ridge, and the Santa Cruz and Vanuatu Islands. The standing waves along the geographically

256   smaller, Loyalty Island ridge vanish for longer-period oscillations at margin and basin scales. Since

257   the oscillation modes are independent of tsunami sources (e.g., Cheung et al., 2013; Aranguiz et

258   al., 2019), the SMART sensors located mostly outside energetic antinodes can record direct

259   tsunami signals with minor influences from adjacent landmasses.
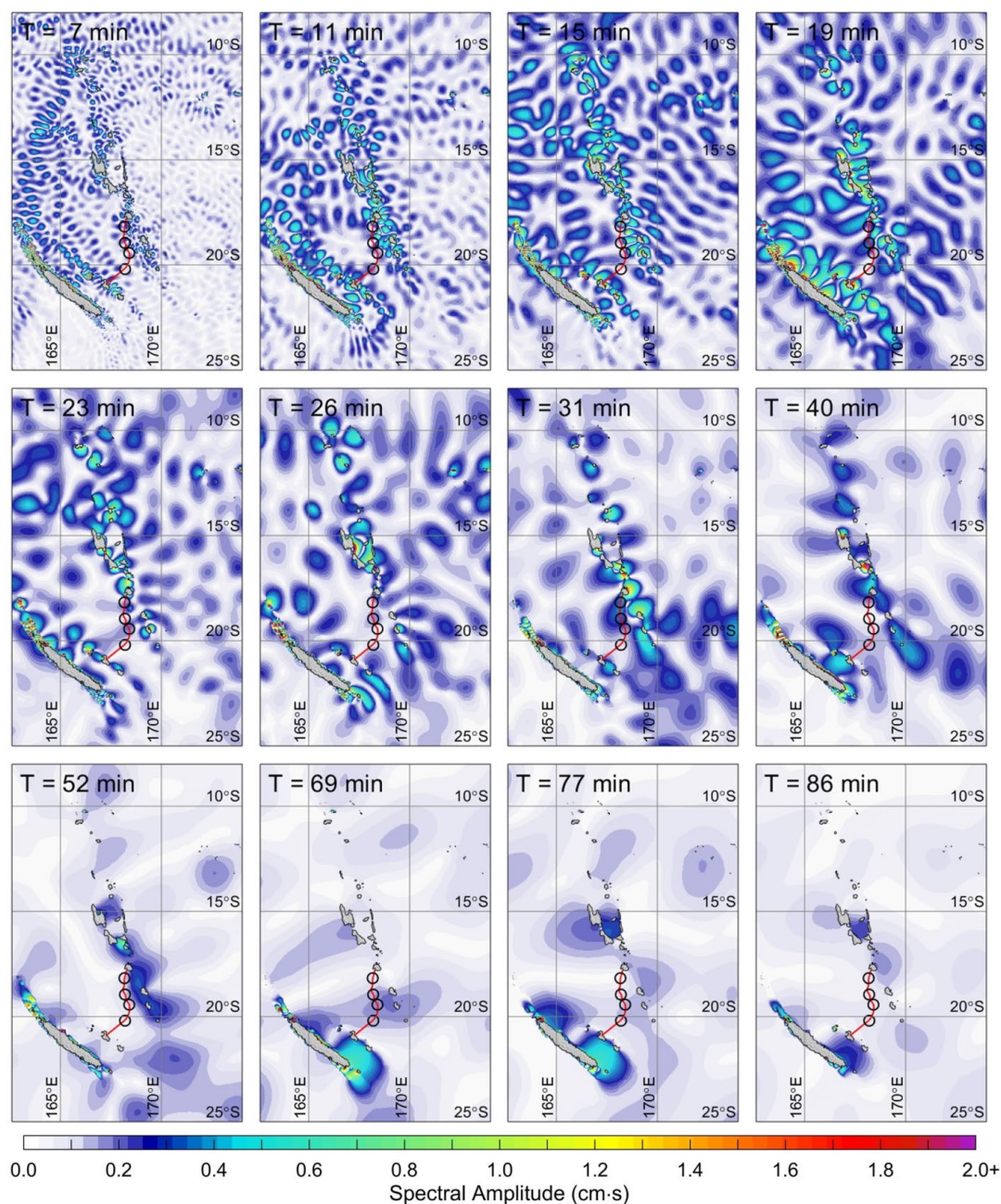
260
261   **Figure 4.** Oscillation modes derived from the 2013 M_W 8.0 Santa Cruz tsunami. Red line and

262   circles denote planned SMART cable and sensor locations.

263   Fig. 5 shows the computed waveforms and spectra from the 2013, 2021, and 2023 tsunamis at

264   sensor 2. All three tsunamis arrive in ~1 hr after earthquake initiation. The 2013 and 2021 thrust

265   faulting events produce initial arrivals in the form of a crest, while the 2023 normal faulting results

266   in a leading trough. The initial arrivals directly from the source via the Vanuatu trench are weak

267   for the 2021 and 2023 events southwest of the Loyalty Islands, because the energy is diverted into

268   the North Fiji Basin through refraction-diffraction across the Hunter Ridge (Robert et al., 2025).

269   The subsequent waveforms are primarily leaked energy from nearby shelf oscillations, where the

270   amplitude is an order of magnitude larger (Fig. 3). The 2013 tsunami from the San Cruz Islands

271   has more energetic long period components due to the sensor's location at 90° azimuth from the

272   main lobe. Despite the varying waveforms in the three events, their spectra show similar sets of

273   harmonics with periods in 10~40 and 50~100 min associated with the island and basin-scale

274   oscillations as shown in Fig 4.

275
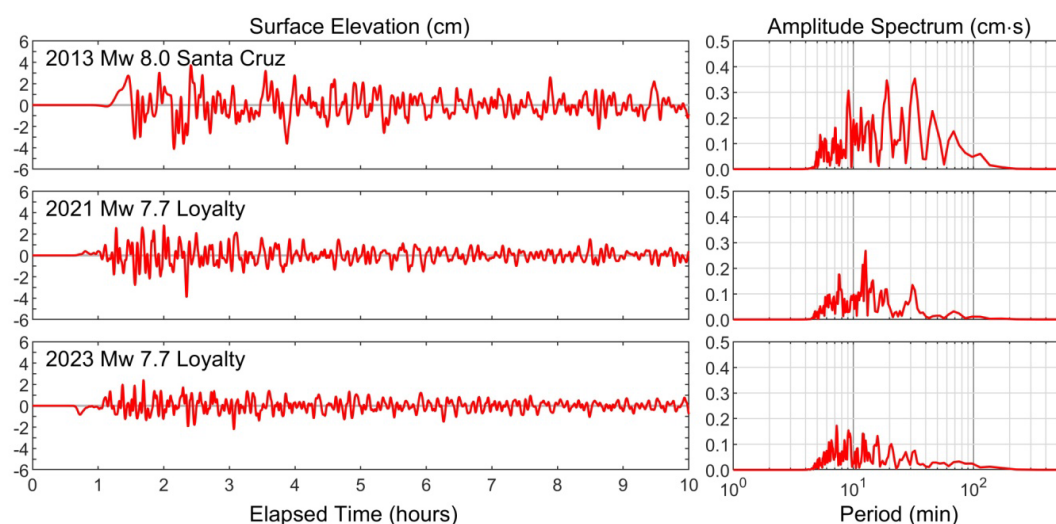
Figure 5. Synthetic tsunami time series and spectra at the target location of SMART sensor 2 from
the three recent major earthquakes in the Vanuatu subduction zone shown in Fig. 2a-c.

278   The vertical and transverse (horizontal perpendicular to the great circle path at the receiver)

279   ground displacements at sensor 2 of the SMART cable are computed for point-source

280   representations of the three major recent ruptures along the Vanuatu subduction zone (Fig. 6). A

281   15-s low-pass filter has been applied to approximately account for temporal finiteness of the

282   ruptures. The arrival times vary with distance from the source to the observing point. Peak ground

283   motions of about 0.2 m are associated with the large Rayleigh wave and Love wave packets on the

284 vertical and transverse components, respectively. The signals include all body wave arrivals. The

285 initial P wave arrives at about 75-120 s after the origin time, when real-time analysis of ground

286 shaking detected at the cable could commence. With a distribution of 4 three-component sensors

287 along the cable, if on-scale recordings are obtained, rapid array processing could determine the

288 azimuth of approach, and initial ground motion amplitudes can be used for magnitude estimation.

289 Surface wave analysis of the larger signals is viable within 150 to 380 s of the earthquake origin

290 time, if low frequency signals are recorded. With tsunami arrivals also varying with source

291 distance, rapid tsunami potential assessment could be commenced using the Tamtam cable

292 observations along with regional and global network observations.

293
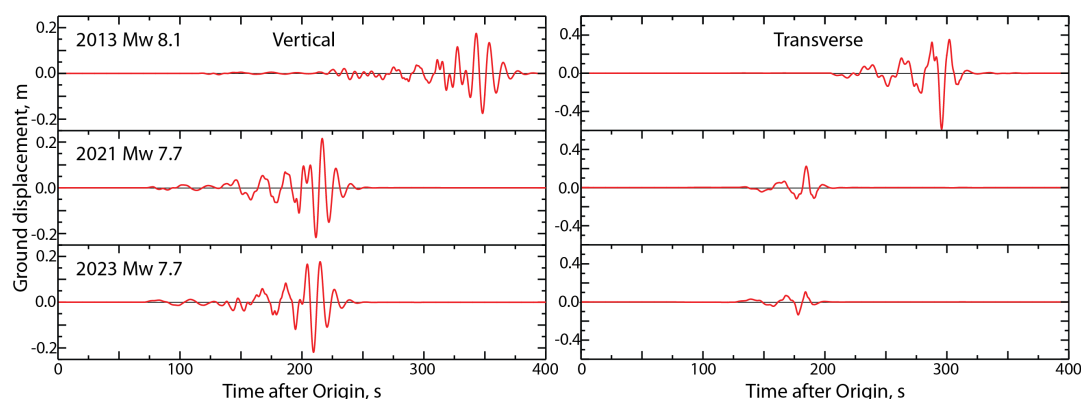
Figure 6. Synthetic ground displacement time series at the target location of SMART sensor 2
from three recent major earthquakes in the Vanuatu subduction zone shown in Fig. 2a-c.

3.2 UNESCO scenarios

297 The UNESCO Mw 8.8 maximum earthquake scenario and its five Mw 8.33 subevents

298 complement the historical events to provide more complete coverage of the parameter space,

299 especially along the most critical southern segment adjacent to population centers. Fig. 7 shows

300 the tsunami wave amplitude along the Vanuatu subduction zone for the six scenarios. The initial

301 wave of the thrust-faulting events is characterized by sea-surface uplift across the margin slope

302 reaching 3.7 m near the trench. Subevent A at the northern end of the segment has the most severe

303 impact to Vanuatu with waves reaching 8.5 m elevation at the east-facing shore of Efate Island,

304 while subevents to the south are more critical to the Loyalty Islands with a maximum elevation of

305 9.3 m at Maré Island (Fig. 7). For the combined Mw 8.8 scenario, the arc curvature focuses the

306 energy toward the southern Vanuatu Islands with nearshore amplification to 11.5 m elevation at

307   Tanna Island. The computed water elevation reaches 12.7 and 11.9 m at Lifou Island and the main

308   island of New Caledonia. Since these values are surface elevations at the shore resolvable by the

309   0.5 arcmin (0.9 km) grid, runup heights might be larger or smaller depending on the coastal terrain.
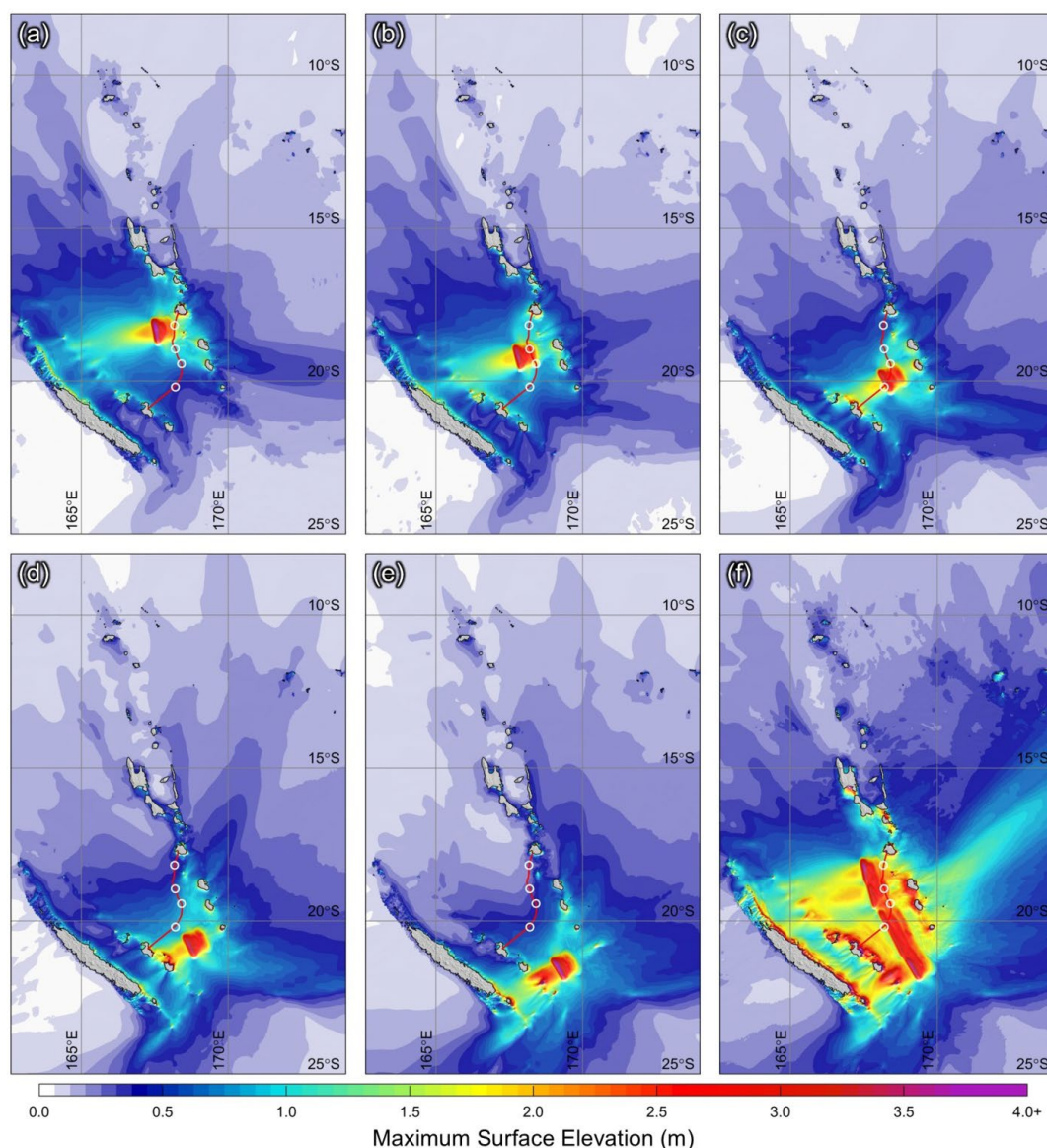
Figure 7. Computed wave amplitude of tsunamis generated by UNESCO earthquake scenarios in Figure 2d. (a) *Mw* 8.33 A earthquake. (b) *Mw* 8.33 B earthquake. (c) *Mw* 8.33 C earthquake. (d) *Mw* 8.33 D earthquake. (e) *Mw* 8.33 E earthquake. (f) *Mw* 8.8 combined maximum earthquake scenario. Red line and circles denote planned locations of the SMART cable and sensors.

315   At least one SMART sensor will be located within the tsunami source regions of subevents A

316   through C as well as the combined event with immediate signature of the initial sea surface uplift.

317   An analysis of the model data shows travel times of 11 and 18 min for the tsunamis sourced from

318   subevents D and E to reach the nearest sensor. Fig. 8 shows the computed waveforms and spectra

319   at sensor 2 from the five subevents and the combined scenario for illustration. The sea surface rises

320   to 2.5 m during the rupture of subevent B directly beneath the sensor, and with only minor energy

321   trapping or resonance over the margin slope, the oscillation subsides rapidly through radiation.

322   Even with rapid wave attenuation outside the source region, the sensor registers direct tsunami

323   signals with less than 1 m amplitude for the other subevents. The combined event has initial wave

324   amplitude similar to subevent B, but the much larger rupture length results in stronger codas due

325   to waves arriving sequentially from the five subevents along the segment. The wave spectra for all

326   six scenarios show strong bimodal, island and basin-scale excitations with peaks closely aligned

327   with the oscillation modes deduced from the 2013 Santa Cruz Island event (Fig. 4).

328
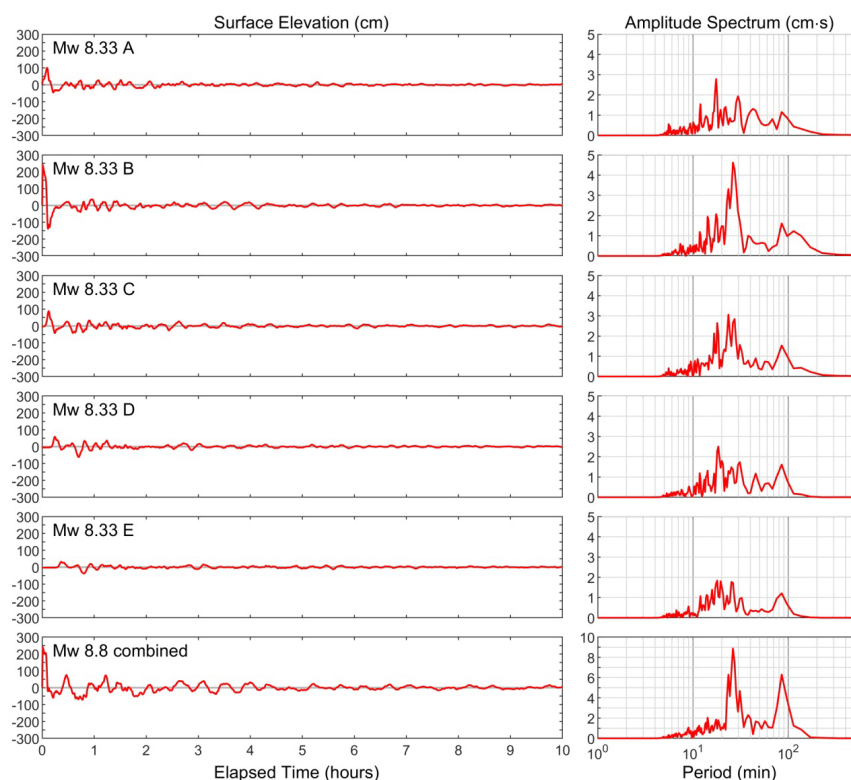
329   **Figure 8.** Synthetic tsunami time series and spectral at the target location of SMART sensor 2 for
330   the UNESCO earthquake scenarios shown in Fig. 2d.

331   The seismic waves at the sensor 2 location are computed for the individual *Mw* 8.33 subevents

332   and the *Mw* 8.8 combined faulting. All scenarios involve 10 m slip with moment tensor point

333   sources at subevent centers and synchronous rupture of the entire segment for simplicity. Fig. 9

334   shows the subevent signals comprising complete seismic ground motions as well as static

335   displacements. A low-pass filter with a 15 s corner has been applied to approximately account for

336   the expected smoothing over the subevent space-time extent. Ground motions are shown for the

337   vertical and transverse components and the time variations between arrivals indicate the distance

338   from subevent centers to the sensor. The strongest seismic waves are produced by subevent B

339   directly beneath the sensor with peak vertical and transverse transient displacements reaching 7 m

340   as well as a static transverse displacement of ~1 m after passage of the large surface waves.
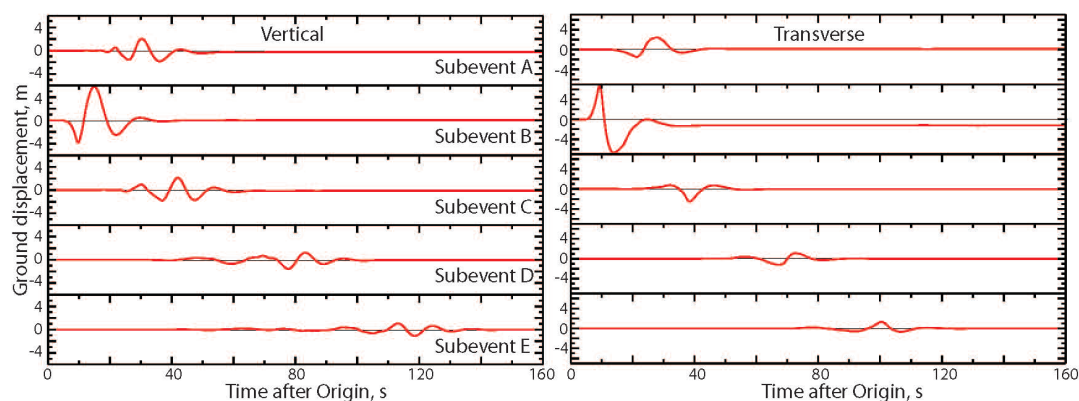
341

342   **Figure 9.** Synthetic ground displacement time series at the target location of SMART sensor 2 for
343   the UNESCO *Mw* 8.33 earthquake scenarios A-E in Fig. 2d. A point-source at the center of each
344   subfault is used for the calculations, and the displacements are low-pass filtered at 15 s period to
345   account for slip duration over the subevent. Vertical and transverse (orthogonal to the great-circle
346   connecting the source and sensor locations) ground displacements are shown.

347   The composite, long duration displacement for the *Mw* 8.8 earthquake scenario is shown in

348   Fig. 10. Since the subevents are assumed to rupture at the same time, their arrivals are delayed by

349   propagation distance alone. The composite ground motions are expressed in terms of the vertical,

350   north-south, and east-west components because the transverse component changes with each

351   subevent location. A 15-s low-pass filter is again applied to approximately account for finiteness

352   of the individual subevents. The sequence of discrete subevent pulses would be smeared out for a

353   true continuous rupture, but the heterogeneous coupling expected along the subduction zone would

354   likely involve correspondingly complex localized failures. The peak ground motion is about 6 m

355   on the vertical and 7.5 m on the horizontal components along with appreciable static displacements

356   due to the sensor location in the rupture zone.

357
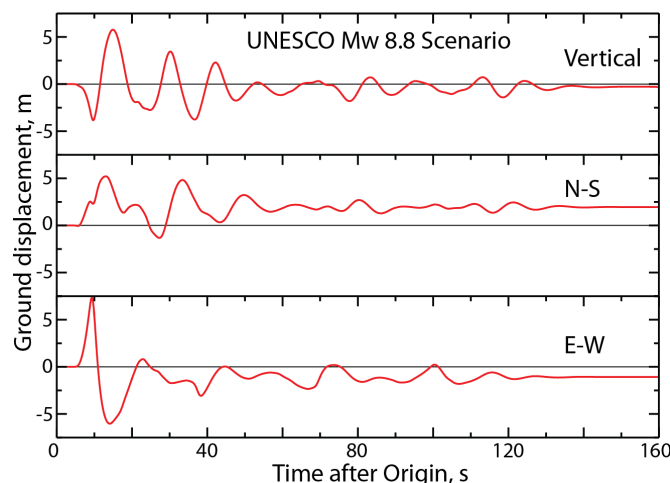
Figure 10. Synthetic ground displacement time series at the target location of SMART sensor 2
for the UNESCO *Mw* 8.8 earthquake scenario in Fig. 2d. For simplicity, the 5 subevents are
assumed to rupture synchronously, and the summed displacements are shown for the vertical,
north-south, and east-west components of motion due to the changing geometry relative to the
target location. A low pass filter at 15 s has been applied.

363   **4. Discussion and Conclusions**

364   Large earthquakes occur along the entire Vanuatu subduction zone exposing many islands in the

365   region to strong ground shaking and tsunami wave impact. Prior studies have systematically

366   examined the hazards and developed fault models for recent major earthquakes and maximum

367   events. These fault models form a basis to develop a plausible range of seismic and tsunami

368   waveforms expected at the Tamtam SMART cable. The results provide a reference for hazard

369   assessment, system and data integration, and emergency management.

370   **4.1 Earthquake and tsunami hazards**

371   There have been 18 shallow (< 70 km deep) *Mw* 7.5+ earthquakes recorded in the Vanuatu

372   subduction zone since 1900 (Cleveland et al., 2014; UNESCO-IOC, 2025). The UNESCO

373   maximum scenario of *Mw* 8.8 provides an upper-bound estimate of potential ground motions and

374   tsunami impacts, but a far-smaller, more frequent major event in the southern segment can still

375   devastate local communities in Vanuatu and New Caledonia. For example, the tsunami generated

376   by the 1875 *Mw* 8.1-8.2 earthquake produced sediment deposits reaching 10 m elevation on the

377   northeastern coast of Lifou Island, New Caledonia (Paris et al., 2023). The impact is comparable

378   to the UNESCO subevents of *Mw* 8.33 with computed sea-surface elevation reaching 8.5 and 9.3

379   m at the shore of Efate Island and Maré Island in Vanuatu and New Caledonia. A recent 17

380   December 2024 *Mw* 7.3 earthquake located 24 km west of Port Vila took 14 lives and injured 265,

381   producing extensive damage in the capital of Vanuatu and long-term impacts on the tourism

382   industry (World Bank, 2025). This event was 54 km deep within the subducting slab, but still

383   produced a 25 cm tsunami. The depth and proximity of such an event to the island leaves little

384   warning times for seismic or tsunami wave arrivals either with or without the Tamtam cable.

385   A major event from the northern or Matthew-Hunter segment, such as the 2013 *Mw* 8.0 and

386   2021 and 2023 *Mw* 7.7 ruptures, also poses earthquake and tsunami hazards in Vanuatu and New

387   Caledonia. The resulting tsunami arrives at the cable locations within an hour after the earthquake

388   allowing limited time to respond if deemed destructive. Hazardous ocean conditions can be long

389   lasting due to amplification and trapping of tsunami energy along island chains (Cheung et al.,

390   2013). The resulting surges might damage ships and disrupt harbor operations despite having

391   minor inundation risks. The limited number of regional seismic and geodetic sensors in operation

392   hampers earthquake and tsunami warning capabilities along the entire subduction zone. The

393   deployment of continuous monitoring along the Tamtam cable may contribute substantially to

394   regional event detection and rapid assessment, particularly along the southern Vanuatu subduction

395   zone.

396   **4.2 Sensor system and data**

397   The seismic, pressure, and temperature sensors are installed inside the repeater housing or in

398   separate modules of submarine telecommunication cables in the case of Tamtam. The broadband

399   seismic sensors and optional accelerometers will be provided by Nanometrics

400   (https://nanometrics.ca), and the temperature and pressure sensors will be supplied by RBR

401   (https://rbr-global.com). The fabrication of sensor modules will be integrated into the cable

402   manufacturing process by Alcatel Submarine Networks (ASN) through its Climate Change Nodes

403   initiative. The collected data from the Tamtam SMART cable will be provided via ASN's Climate

404   Change Portal for low-latency distribution to hazards monitoring agencies, such as the Vanuatu

405   Meteorological and Geohazards Department (VMGD), Oceania Regional Seismic Network

406   (ORSNET), and for long-term storage and dissemination for further analysis and climate research

407   via Ifremer (French Research Institute for Exploitation of the Sea).

408   With tsunami waves arriving well after seismic waves, rapid tsunami potential assessment
409   could be commenced using the cable seismic observations along with regional and global land-
410   based seismic network records. The spectral analysis has shown recorded tsunamis signals from
411   sensors placed outside insular shelves have minor effects from resonance oscillations to provide
412   general indications of potential impact and confirm inferences from seismic observations. Caution
413   must be exercised for earthquake sources near the sensors. Large dynamic ground displacement
414   might interfere with operations of motion sensors laid on sediments. Lacking specific knowledge
415   of the short-period ground displacements and the associated ground velocities and accelerations,
416   we do not attempt to predict the actual recording fidelity of the Tamtam sensors, but after
417   deployment, ground motion models can quickly be developed for the paths around the stations.
418   Also not considered in this study is seismic noise in water level records that might mask initial
419   tsunami arrivals as commonly seen in bottom pressure data from DART stations near earthquake
420   sources (e.g., Bai et al., 2022, 2023). Additional QA/QC and post-processing are warranted as part
421   of automated data analysis (e.g., An et al., 2017).

4.3 Emergency management

423   Vanuatu is an island nation in the Southwest Pacific with an 800-900 km long archipelago of
424   83 islands. The Vanuatu Meteorology and Geohazards Department (VMGD) is the government
425   institute with the mandate to monitor meteorological and geological hazards, including volcanoes,
426   earthquakes, and tsunamis, and provide early warning updates to the public. VMGD has an
427   established geological monitoring network consisting of 15 plus seismic monitoring stations
428   scattered along the six provinces of Vanuatu. Broadband sensors and established telemetry
429   transmission to the VMGD data center enables near real time seismic event detection. The
430   installation of tide gauges near the coastline of some islands assists with tsunami monitoring.
431   However, the detection range is localized to Vanuatu region and does not extend regionally or to
432   the subduction zone.

433   The National Disaster Management Office (NDMO) is responsible for the response and
434   recovery to any disaster and activation of the National Emergency Operations Center with the
435   advice from VMGD. Having a well-established hierarchy of groups down to province and
436   community levels allows coordinated pre-disaster awareness and outreach efforts and transfer of
437   response and recovery efforts to the government and partners post disaster. The effectiveness of
438   preparedness and mitigation measures developed is a result of the availability of the real-time

439   seismic and historical data possessed by VMGD. The latter is now augmented here by synthetic

440   seismic and tsunami data from three recent major earthquakes and tsunamis as well as the

441   UNESCO-IOC maximum scenario along with its subevents for hazard assessment and long-term

442   planning.

443   The deployment of the Tamtam SMART cable and integration of its real-time data into

444   VMGD's monitoring system will greatly enhance the current early warning system. The Vanuatu

445   subduction zone has so far been lacking direct observation since there has never been monitoring

446   equipment installed in the area. The seismic, temperature and pressure data that will be made

447   available by the four proposed ASN Climate Change Nodes will feed additional information to the

448   current system providing earthquake detection parameters and tsunami threat analysis in and

449   around the subduction zone. Acquiring such data will support preparedness and mitigation efforts

450   developed by NDMO resulting in a well informed and prepared country. The benefits will extend

451   to the southwest Pacific and will be of great interest to the research community as well.

452   *Code availability.* The NEOWAVE code for tsunami modeling may be requested from the

453   corresponding author for academic research. The SYNGINE seismic wave simulator is available

454   online (https://ds.iris.edu/ds/products/ondemandsynthetics/).

455   *Data availability.* The digital elevation model used in this study is available at GEBCO

456   (https://www.gebco.net/data_and_products/gridded_bathymetry_data/).

457   *Authorship contribution.* KC: Conceptualization, Methodology, Investigation, Project

458   Administration, Writing - original draft, review and editing. YY: Methodology, Investigation,

459   Software, Formal analysis, Data curation, Visualization, Writing - review and editing. TL:

460   Methodology, Investigation, Software, Formal analysis, Data curation, Visualization, Writing -

461   original draft review and editing. MF: Writing - original draft, review and editing. JN: Writing -

462   original draft, review and editing. BH: Writing - review and editing.

463   *Declaration of competing interest.* The authors declare that they have no known competing

464   financial interests or personal relationships that could have appeared to influence the work reported

465   in this paper.

466   *Acknowledgements.* SOEST Contribution No. XXXXX.

Financial support. The Gordon and Betty Moore Foundation funded this study through Grant No. GBMF10787 to the University of Hawaii and subawards to Subsea Data Systems and Vanuatu Meteorology and Geo-hazards Department. T. Lay was supported by the National Science Foundation under grant number EAR-1802364.

References

An, C., Cai, C., Zheng, Y., Meng, L, Liu, P.: Theoretical solution and applications of ocean bottom pressure induced by seismic seafloor motion. Geophys. Res. Lett., 44, 10,272-10,281, doi:10.1002/2017GL075137, 2017.

Aranguiz, R., Catalán, P.A., Cecioni, C., Bellotti, G., Henriquez, P., and González, J. Tsunami resonance and spatial pattern of natural oscillation modes with multiple resonators. J. Geophys. Res.: Oceans, 124, 7797-7816, doi:10 .1029/2019JC015206, 2019.

Bai, Y., Liu, C., Lay, T., Cheung, K.F., and Ye, L.: Optimizing a model of coseismic rupture for the 22 July 2020 M_W 7.8 Simeonof earthquake by exploiting acute sensitivity of tsunami excitation across the shelf break. J. Geophys. Res.: Solid Earth, 127, e2022JB024484, doi:10.1029/2022JB024484, 2022.

Bai, Y., Liu, C., Lay, T., Cheung, K.F., and Yamazaki, Y.: Fast and slow intraplate ruptures during the 19 October 2020 magnitude 7.6 Shumagin earthquake. Nat. Comm., 14(1), 2015, doi:10.1038/s41467-023-37731-2, 2023.

Bai, Y., Yamazaki, Y, and Cheung, K.F.: Intercomparison of hydrostatic and nonydrostatic modeling for tsunami inundation mapping. Phys. Fluids, 35(7), 077111, doi:10.1063/5.0152104, 2023b.

Cheung, K.F., Bai, Y., and Yamazaki, Y.: Surges around the Hawaiian Islands from the 2011 Tohoku tsunami. J. Geophys. Res. Oceans, 118(10), 5703-5719, doi:10.1002/jgrc.20413, 2013.

Cleveland, K.M., Ammon, C.J., and Lay, T.: Large earthquake processes in the northern Vanuatu subduction zone, *J. Geophys. Res.: Solid Earth*, 119, 8866-8883, doi:101002/2014JB011289, 2014.

Davies, G. and Griffin, J.: The 2018 Australian Probabilistic Tsunami Hazard Assessment. Record 2018/41, Geoscience Australia, Canberra, https://doi.org/10.11636/Record.2018.041, 2018.

Dziewonski, A.M. and Anderson, D.L.: Preliminary reference Earth model. Phys. Earth Planet. Int., 25, 297-356, doi:10.1016/0031-9201(81)90046-7, 1981

Fry, B., McCurrach, S.-J., Gledhill, K., Power, W., Williams, M., Angove, M., Arcas, D. and Moore, C.: Sensor network warns of stealth tsunamis. Eos, 101, doi:10.1029/2020EO144274, 2020.

Heidarzadeh, M., Harada, T., Satake, K., Ishibe, T., and Gusman, A.R.: Comparative study of two tsunamigenic earthquakes in the Solomon Islands: 2015 Mw 7.0 normal-fault and 2013 Santa Cruz Mw 8.0 megathrust earthquakes. Geophys. Res. Lett., 43(9), 4340-4349, doi:10.1002/2016GL068601, 2016.

Howe et al.: SMART cables for observing the global ocean: science and implementation. Front. Earth Sci., 6, 424, doi:10.3389/fmars.2019.00424, 2019.

Howe et al.: SMART subsea cables for observing the earth and ocean, mitigating environmental hazards, and supporting the blue economy. Front. Earth Sci., 9, 775544, doi:10.3389/feart.2021.775544, 2022.

Lay, T., Ye, L., Kanamori, H., Yamazaki, Y., Cheung, K.F., and Ammon, C. J.: The February 6, 2013 Mw 8.0 Santa Cruz Islands earthquake and tsunami. Tectonophysics, 608, 1109–1121, doi:10.1016/j.tecto.2013.07.001, 2013.

Li, L. and Cheung, K.F.: Numerical dispersion in non-hydrostatic modeling of long-wave propagation. Ocean Modell., 138, 68-87, doi:10.1016/j.ocemod.2019.05.002, 2019.

Ioualalen, M., Pelletier, B., and Solis Gordillo, G.: Investigating the March 28th 1875 and the September 20th 1920 earthquakes/tsunamis of the Southern Vanuatu arc, offshore Loyalty Islands, New Caledonia. Tectonophysics, 709, 20–38, doi:j.tecto.2017.05.006, 2017.

Okada, Y.: Surface deformation due to shear and tensile faults in a half-space. Bull. Seismol. Soc. Am., 75(4), 1125-1154, doi:10.1785/BSSA0750041135, 1985.

Paris, R, Pelletier, B., Roger, J., Wassmer, P., and Sabatier, P.: Sedimentary evidence of tsunamis in New Caledonia, southwest Pacific. Mar. Geol., 463, 107116, doi:10.1016/j.margeo.2023.107116, 2013.

Robert, W.H., Yamazaki, Y., Cheung, K.F., and Lay, T.: Tsunami variability for the 2021 megathrust and 2023 outer rise Mw 7.7 earthquake southeast of the Loyalty Islands. J. Geophys. Res.: Oceans, 130, e2024JC021880, doi:10.1029/2024JC021880, 2025.

526 Roger, J. and Pelletier, B.: A brief history of tsunamis in the Vanuatu Arc. Nat. Haz. Earth Syst.
527   Sci., 24(10), 3461-3478 doi:10.5194/nhess-24-3461-2024, 2024.

528 Roger, J.H.J., Pelletier, B., Duphil, M., Lefévre, J., Aucan, J., Lebellegard, P, Thomas, B.
529   Bachelier, D., and Varillon, D.: The M_W 7.5 Tadine (Maré, Loyalty Islands) earthquake and
530   related tsunami of 5 December 2018: seismotectonic context and numerical modeling. Nat.
531   Haz. Earth Syst. Sci., 21(11), 3489-3508, doi:10.5194/nhess-21-3489-2021, 2021.

532 Tanioka, Y. and Satake, K.: Tsunami generation by horizontal displacement of ocean bottom.
533   Geophys. Res. Lett., 23(8), 861-864, doi:10.1029/96GL00736, 1996.

534 UNESCO-IOC: Expert Meeting on Tsunami Sources, Hazards, Risk and Uncertainties Associated
535   with the Vanuatu, Solomon and New Britain Subduction Zones, Port Vila, Vanuatu, 14-17
536   May   2024.   Workshop   Report   315,   UNESCO,   Paris,   France.
537   https://unesdoc.unesco.org/ark:/48223/pf0000392442.locale=en, 2025.

538 World Bank: Global Rapid Post-Disaster Damage Estimation Report: The December 17, 2024 Mw
539   7.3 Earthquake in Port Vila, Vanuatu. Global Facility for Disaster Reduction and Recovery,
540   World Bank, Washington, DC, http://hdl.handle.net/10986/42820, 2025.

541 Yamazaki, Y., Bai, Y., Goo, L.L., Cheung, K.F., and Lay, T.: Nonhydrostatic modeling of
542   tsunamis from earthquake rupture to coastal impacts. J. Hydraul. Eng., 149(9), 04023033,
543   doi:10.1061/JHEND8.HYENG-133, 2023.

544 Yamazaki, Y., Cheung, K.F., and Kowalik, Z.: Depth-integrated, non-hydrostatic model with grid
545   nesting for tsunami generation, propagation, and run-up. Int. J. Numer. Meth. Fluids, 67, 2081-
546   2107, doi:10.1002/fld.2485, 2011.

547 Yamazaki, Y., Kowalik, Z., and Cheung, K.F.: Depth-integrated, non-hydrostatic model for wave
548   breaking and run-up. Int. J. Num. Meth. Fluids, 61, 473-497, doi:10.1002/fld.1952, 2009.

549 Ye, L., Gong, W., Lay, T., Kanamori, H., and Chen, X.: Shallow megathrust rupture during the 10
550   February 2021 M_W 7.7 Southeast Loyalty Islands Earthquake Sequence. Seism. Rec., 1(3),
551   154–163, doi:10.1785/0320210035, 2021.